

DERIVING A UNIFIED SPACE OBJECT CATALOGUE FOR THE PURPOSE OF SPACE DEBRIS MONITORING AND MODELLING

E. Stevenson, S. Lemmens, and J. Siminski

ESA/ESOC, Robert-Bosch-Str. 5, 64293 Darmstadt, Germany,
Email: emma.stevenson@esa.int, stijm.lemmens@esa.int, jan.siminski@esa.int

ABSTRACT

A framework has been developed for deriving a unified space object catalogue, from distinct and operationally used source catalogues.

For combining complementary measurements, the method of covariance intersection was investigated. As many of the datasets concerned will have unknown generation parameters, an estimate of the orbital state and its covariance, must first be obtained by refitting them to a common force model. To up-scale this orbit determination process to whole catalogues, characteristic length of update intervals (LUIs), were explored for subclasses of objects. It was found that high fidelity orbit classes yielded the most representative and differentiable results for this purpose. Using these optimised LUIs, covariance intersection is then performed for a GTO test case.

For this study, CSpOC Special Perturbation (SP) data and JSC Vimpel data are considered, though the framework is flexible to expansion.

Keywords: Space Catalogue; Orbit Determination; Space Safety; Space Debris.

1. INTRODUCTION

Within the realm of space safety, access to accurate, up-to-date and comprehensive orbital information of objects that may pose a collision risk, as well as the space debris environment as a whole, is fundamental in ensuring the protection of in-space infrastructure. Unifying such data from existing catalogues, based on individual surveillance and tracking networks of different observational capabilities, would enable as extensive a set of objects as possible to be maintained. This may then be employed in space situational awareness activities, such as collision avoidance, re-entry risk assessment and mapping of the future environment.

At ESA, these activities are conducted using orbital data from ESAs Database and Information System Character-

ising Objects in Space (DISCOS), largely based on information provided by the US Combined Space Operations Centre (CSpOC). Data from external catalogues such as this, are stored within DISCOS in the same frame and format as their catalogue of origin [8]. This catalogue independence allows new data sources to be easily incorporated, and has already been extended to include states from JSC Vimpel Space Objects, which have been provided since 2014 [7] (Figure 1). The Vimpel dataset includes highly eccentric and geosynchronous objects, many of which are untracked by CSpOC. However, differing formats and unknown generation parameters preclude the integration of all datasets into a single catalogue.

The aim of this work is thus to begin to develop a framework for deriving a unified space object catalogue, from distinct and operationally used source catalogues, to be ultimately incorporated into DISCOS. For this study, CSpOC Special Perturbation (SP) data and the aforementioned Vimpel data will be considered, though the framework is flexible to further expansion.

For fusing data of different formats, frames and force models, the method of covariance intersection (CI) is investigated. But first, an estimate of the orbital state and a measure of its covariance must be obtained by refitting the data to a common force model. To upscale this process for whole object catalogue, representative orbit determination (OD) controls for subsets of objects are explored, specifically that of the OD arc length, or length of update interval (LUI).

The set-up of the paper is as follows. Section 2 contains a review of how different perturbative effects may be used to characterise an orbit, and how this may be used to define a binning methodology for optimising catalogue maintenance. Information on the considered datasets and any prior knowledge of their force models is then given in Section 3, before a description of the optimisation process used to determine optimal OD controls for the subsets in Section 4. Once these have been established, a discussion of the fusion of correlated data using CI is given in Section 5 via a test case.

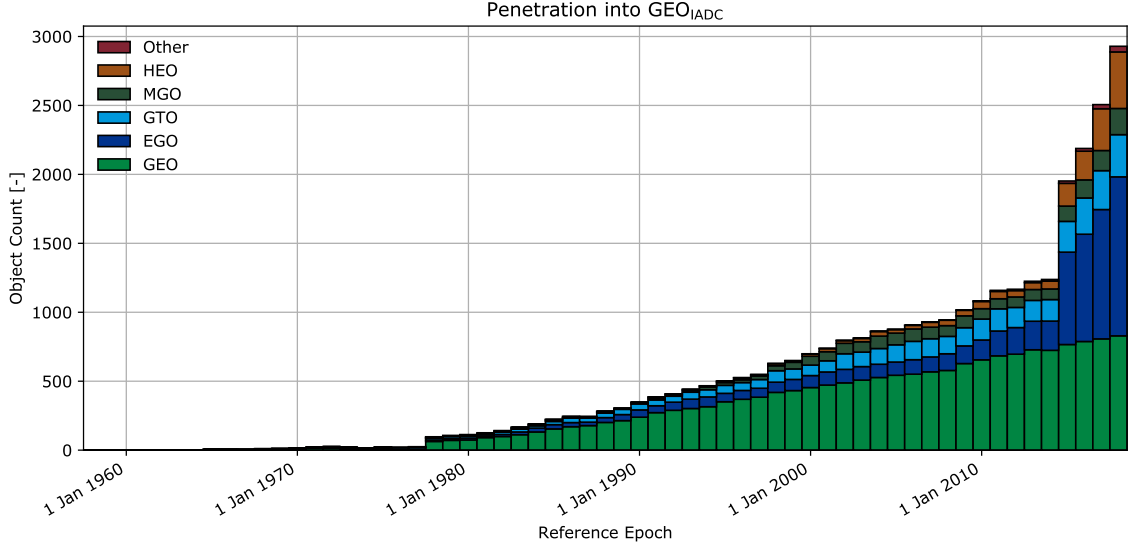


Figure 1. Evolution of absolute number of objects infringing upon GEO protected region [4]. Definitions of orbital regions given in Table 3. Increase in object count in 2014 due to inclusion of Vimpel catalogue.

2. SATELLITE TAXONOMY

In order to simplify the OD process used during cataloguing, space objects can be divided into groups that have similar orbital properties. OD control parameters can then be optimised for a representative class of objects, rather than individually, resulting in a more manageable and less computationally intensive process.

Satellites may be classified by the extent to which they experience different perturbative effects, as this will directly impact the requirements for maintaining orbital element sets. The perturbing effects acting on the orbital dynamics of an object are comprised within a force model.

2.1. Force Models

The equations of motion of an object, which will be solved by the OD process, are composed from models of which forces act upon a satellite. At the most basic level, the orbital dynamics are modelled by a Keplerian orbit, dependent only on the central Earth gravity field. Additional corrections to the force model, or perturbations, include the following [10]:

- Non-spherical Earth gravity field: acceleration due to asphericity of Earth's geopotential. The gravity field may be described by a series of coefficients, $J_{n,m}$, derived from an expansion in spherical harmonics of the Earth's internal mass distribution.
- Third body perturbations: gravitational interactions with the Sun, Moon, planets, asteroids as well as relativistic corrections and lunisolar torques.

- Atmospheric resistance: drag, lift and binormal. Deceleration due to drag resistance, the primary contributing factor, may be described by,

$$\ddot{\vec{r}} = -\frac{1}{2}C_D \frac{A}{m} \rho v_r^2 \vec{v}_r \quad (1)$$

where \vec{v}_r is the radial satellite velocity, A is the frontal area of the satellite exposed to the particle flux (thus requiring attitude knowledge), and M , the satellite mass. C_d , the drag coefficient, describes the interaction of the atmospheric constituents with the satellite's surface material. The combination of these physical parameters, $C_d A/m$, form the ballistic coefficient. ρ is the neutral atmospheric density at the satellite's location, thus requiring modelling of the properties and dynamics of the Earth's atmosphere, and therefore knowledge of solar and geomagnetic activity. On account of these many uncertainties, the atmosphere model is the least consistently modelled perturbation, and hence likely to be the major difference in force models of alternative catalogues.

- Solar radiation pressure (SRP): momentum imparted by the reflection or absorption of photons,

$$\ddot{\vec{r}} = -P_{\odot} C_R \frac{A}{m} \frac{\vec{r}_s}{r_s^3} \quad (2)$$

where P_{\odot} represents the solar radiation pressure, C_r the radiation pressure coefficient (a measure of the absorptivity of satellite surface), and A the effective surface area exposed to the solar radiation. \vec{r}_s is the satellite position relative to the sun. Additional corrections may include eclipse conditions, occultations, and shadow transits.

- Thrust forces: satellite imparted orbit, or attitude, control.
- Minor perturbations: Earth radiation pressure (albedo), Earth tides and relativistic effects.

So as not to unnecessarily exceed the accuracy of available tracking networks, force models typically only account for perturbations on the order of several centimetres, neglecting the above mentioned minor perturbations.

2.2. Classification Schemes

Typical taxonomic schemas focused on division by orbital regime or class, for example using Gabbard Classes, in which bin in the apogee and perigee height of the orbit in order to account for the effects of atmospheric drag. In [2], groups are alternatively based on Two Line Element set (TLE) mean motion, eccentricity and inclination.

This approach was extended in [5], [6] in which additional sub-divisions, based on the non-conservative forces that affect the orbit, were introduced to capture further differences in orbital maintenance properties.

In the low earth (LEO) and highly eccentric (HEO) orbital regimes, atmospheric drag is this primary additional driver. Although characterisation by the geometric properties of the orbit alone accounts for differences in atmospheric density, ρ , the drag force affecting the orbital motion of an object is also affected by its physical properties, $C_d A/m$ (Equation 1). To account for both of these factors, a subdivision schema (Table 1) was introduced in energy dissipation rate (EDR),

$$EDR = -\frac{1}{T} \int_{s_1}^{s_2} \vec{a}_D \cdot d\vec{s} \quad (3)$$

$$= -\vec{a}_D \cdot \vec{v} \quad (4)$$

where T is the time interval from point s_1 to s_2 , $d\vec{s}$ is the differential arclength along the orbit, and \vec{a}_D is the drag acceleration, which acts in the anti-velocity direction. EDR is a measure of the amount of energy being removed from the orbit and, as such, the amount of atmospheric drag that a satellite experiences. As \vec{a}_D follows Equation 1, the EDR is dependent on both the physical properties of the satellite, as well as the solar conditions affecting ρ .

The EDR bins (Table 1) are spaced at an approximately constant logarithmic separation in bin averaged state vector error [6]. They represent different levels of severity for the atmospheric drag retarding force, with 0 including satellites which experiencing no atmospheric drag, and 10, the most severe.

Higher drag bins are excluded for geostationary (GEO) and medium earth orbit (MEO) satellites due to their

Table 1. EDR subdivision schema (aggregated from that used in [5])

Bin	EDR Bounds [W/kg]
0	$0 \leq \leq 0.0006$
1	$0.0006 < \leq 0.0020$
2	$0.0020 < \leq 0.0090$
3	$0.0090 <$

Table 2. Solar Radiation Coefficient bins as recommended in [6].

Bin	$C_r A/M$ Bounds [m^2/kg]
0	$0 \leq < 0.014$
1	$0.014 \leq$

altitude. In this regime, the principal non-conservative force is that of SRP. A further subdivision for EDR bin 0 is therefore also introduced, analogous to that of atmospheric drag, to account for SRP susceptibility. This is given in Table 2. Here, P_\odot and r_s scale consistently so only the physical properties of the satellite need to be accounted for: $C_r A/m$ (Equation 2) [6].

The orbital regimes implemented in this work are taken from the working Space Debris Office (SDO) definitions, defined in Table 3.

3. SOURCE CATALOGUES

3.1. CSpOC Special Perturbation Data

The US Space Catalogue, generated using optical and radar measurements from the Space Surveillance Network (SSN), is maintained by CSpOC [9]. The Special Perturbation (SP) ephemerides are obtained from a numerical OD process, solved for a higher level force model than that used for the generation of TLE sets. They are provided daily, with each ephemeris spanning ~ 4 days.

A different approach to the modelling of drag effects in the force model is implemented, in the form of a Dynamic Calibration Atmosphere (DCA). This is part of the High Accuracy Satellite Drag Model (HASDM) [12]. The DCA dynamically estimates ρ near real-time, directly from the SSN. In this process, drag information is determined from tracking observations of a set of inactive low-perigee calibration satellites.

Table 3. ESA orbital class definitions, with semi-major axis a , eccentricity e , inclination i , perigee height h_p and apogee height h_a given in [km] and [deg] [4].

Orbit	Description	Definition		
GEO	Geostationary Orbit	$i \in [0, 25]$	$h_p \in [35586, 35986]$	$h_a \in [35586, 35986]$
IGO	Inclined Geosynchronous Orbit	$a \in [37948, 46380]$	$e \in [0.00, 0.25]$	$i \in [25, 180]$
EGO	Extended Geostationary Orbit	$a \in [37948, 46380]$	$e \in [0.00, 0.25]$	$i \in [0, 25]$
NSO	Navigation Satellites Orbit	$i \in [50, 70]$	$h_p \in [18100, 24300]$	$h_a \in [18100, 24300]$
GTO	GEO Transfer Orbit	$i \in [0, 90]$	$h_p \in [0, 2000]$	$h_a \in [31570, 40002]$
MEO	Medium Earth Orbit	$h_p \in [2000, 31570]$	$h_a \in [2000, 31570]$	
GHO	GEO-superGEO Crossing Orbits	$h_p \in [31570, 40002]$	$h_a > 40002$	
LEO	Low Earth Orbit	$h_p \in [0, 2000]$	$h_a \in [0, 2000]$	
HAO	High Altitude Earth Orbit	$h_p > 40002$	$h_a > 40002$	
MGO	MEO-GEO Crossing Orbits	$h_p \in [2000, 31570]$	$h_a \in [31570, 40002]$	
HEO	Highly Eccentric Earth Orbit	$h_p \in [0, 31570]$	$h_a > 40002$	
LMO	LEO-MEO Crossing Orbits	$h_p \in [0, 2000]$	$h_a \in [2000, 31570]$	
UFO	Undefined Orbit			
ESO	Escape Orbits			

3.2. JSC Vimpel Data

Since 2014, orbital data from a Russian object catalogue, maintained by JSC Vimpel Interstate Corporation and Keldysh Institute of Applied Mathematics (KIAM) (henceforth denoted as the Vimpel Catalogue), has been made publicly available [7]. This encompasses orbital data obtained from optical measurements (including the International Space Observation Network (ISON)).

The primary focus of this catalogue is objects with orbital period exceeding 200 minutes. This regime, primarily focussing on HEO and GEO objects, is tasked less by the SSN and as such compliments the CSPOC SP catalogue. Object correlations between the two catalogues are provided alongside the Vimpel data, and are additionally updated by a SDO internal correlation tool. At present, around 500 of the ~ 4500 Vimpel objects have been correlated with TLE objects.

The Vimpel catalogue provides orbital and physical parameter estimates for each object at approximately 7 day intervals, including the effective area-to-mass ratio. Ephemerides are additionally provided for objects with sufficient orbital accuracy for the next 7 days. These are generated using the Russian standard atmosphere model GOST (R 25645.166-2004).

4. LUPI OPTIMISATION

As discussed in Section 2, the OD controls for the cataloguing process may be optimised for a similarly representative group.

In previous studies, for each class, a recommended update interval for the batch least-squares used during the OD, and number of observations per day, was given to maintain the accuracy of a given satellite element set [2], [9]. However, in these cases, only a few observations were available per day. Thus, the compromise between

reducing the covariance and having the capability to accurately represent the dynamics, is different to that which should be applied to ephemeris data, where (pseudo) observations are available roughly every 10 minutes.

As the observation frequency is set, we focus on the time span of the batch least squares process, the OD arc length, or LUPI.

4.1. Procedure

In the SDO, OD used for the purposes of generating conjunction forecasts and collision risk estimates, is performed independently from the SSN, using the ODIN (Orbit Determination via Improved Normal Equations) tool [1]. By effectively re-fitting, in an OD sense, to ephemeris data, we obtain a measure of how well the force model dynamics align. This was investigated with increasing arc length, where the start of the ephemeris was fixed to the start of the LUPI.

To identify the regime of arc lengths in which the OD yields physical results, two limits must be accounted for: a lower limit for which the state is still stabilising, where only a few measurements are available; and an upper limit where, in some cases, the state will drift away from previous estimates. This trade-off is demonstrated in Figure 2. Here, the estimated sigma is unduly optimistic, as it assumes that the force model differences may be described by a normal distribution, and that the errors are uncorrelated.

From this, we can determine the largest possible fit interval which is well approximated by the ODIN dynamics. However, this quantity may additionally be constrained by a limiting requirement on the fit residuals.

The force model implemented by ODIN for this analysis was as follows:

- Non-central gravity field using Joint Earth Gravity

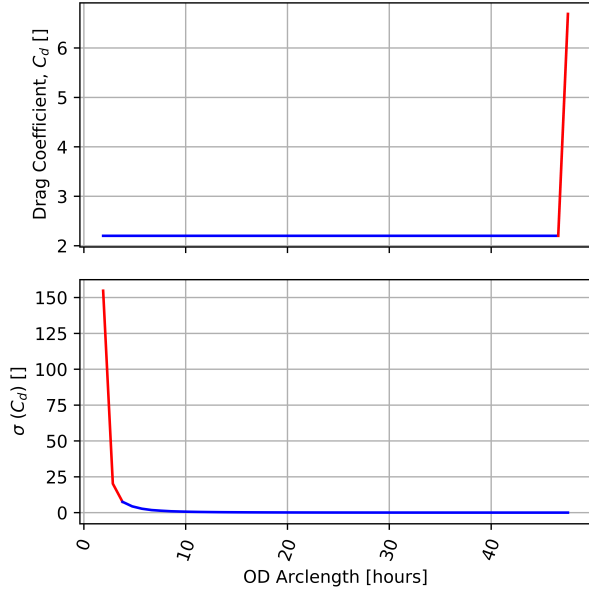


Figure 2. Evolution of C_d and $\sigma(C_d)$ with LUPI for NO-RAD object 37875 (a Chinese Earth observation satellite, in the high drag LEO regime). ‘Stable’ region represented in blue, and ‘drift’ in red.

model (JGM) 3 with degree, order 30×30 .

- Third body point-mass gravitation of the Sun and Moon.
- NRLMSIS-00 air density model.
- SRP using the conical shadow model (umbra and penumbra).

For the example of satellite RapidEye 1, for which SDO provides a collision avoidance service using global positioning system data [11], the evolution of estimated parameters and RMS is shown in Figure 3. Ideally, for operational use, the RMS should be limited to a few metres. The usable set of LUPIs is therefore constrained between approximately 5, after which the state stabilises, and 10 hours.

The objective of the optimisation procedure is thus to find the largest possible OD arc before state drift, subject to RMS constraints. The upper bound was investigated to ensure that a viable LUPI would be available that exceeded the update frequency of the ephemerides.

For the procedure to be easily extendible to orbital ephemerides with varied generation parameters, it is required to be as robust, and hence uncomplicated, as possible. A statistical certainty should also be assigned to the optimal point, to allow for the identification of representative objects per bin. The procedure used is as follows.

To identify the lower limit, after which we assume the state stabilises, the convergence of the sigma estimation of the estimated elements (Keplerian orbital elements,

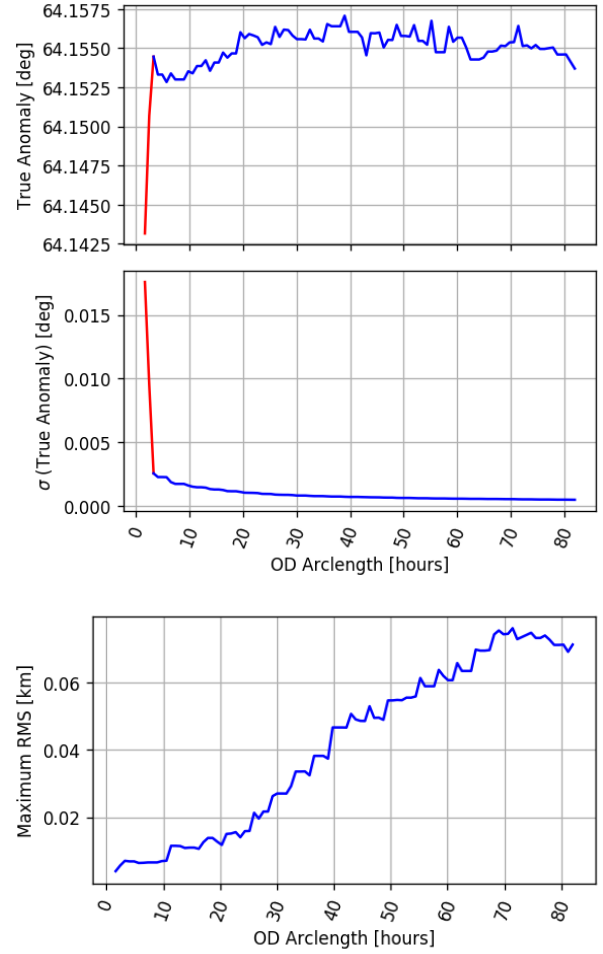


Figure 3. LUPI evolution with estimated true anomaly and its corresponding sigma value, and maximum RMS of the OD fit for RapidEye 1 GPS measurement data. ‘Stable’ region represented in blue, and initial stabilisation in red.

C_d, C_r) is exploited. The inflexion point of the sigma decay is identified, and the region before is discounted.

To identify an upper limit, a univariate statistical test for detecting outliers was implemented for the estimated orbital elements, residuals, and number of OD iterations required for convergence:

1. A Grubbs’ test, based on the Student t-distribution, is performed over each dataset with null hypothesis, H_0 , that no outliers are present. The statistic, G , represents the largest absolute deviation from the sample mean in units of the sample standard deviation. The α for which H_0 is rejected (when Equation 6 holds) for a given data point is stored before the outlier is removed for the next iteration. N is the number of data points, σ is the standard deviation, and $t_{\alpha/2N, N-2}$ is the value of the t-distribution with $N - 2$ degrees of freedom, and a significance level

of $\alpha/2N$.

$$G = \frac{\max_{i=1,\dots,N} |x_i - \bar{x}|}{\sigma} \quad (5)$$

$$G > \frac{N-1}{\sqrt{N}} \sqrt{\frac{t_{\alpha/2N, N-2}^2}{N-2 + t_{\alpha/2N, N-2}^2}} \quad (6)$$

2. In order to determine a metric for stability over all variables, the data was discretised into LUPI bins (typically spanning 1-2 orbital periods). Considering each variable individually, this allows for the classification of *drift* or *spike* behavioural regions over increasing LUPI (examples of this are given in Figures 2 and 3). The α level with which the outliers were identified was summed over each bin. The cumulative value of each LUPI bin, weighted over all variables, could then be used. An absolute limit on fluctuation size from which an outlier could contribute was taken to be 10^{-5} .
3. The upper limit of the dataset was constrained to a limiting RMS.
4. The above metric gives a confidence measure as to whether a region in OD arclength is *stable*. The optimum LUPI (upperbound) is therefore taken as the largest arclength with smallest summed significance.

This optimal LUPI was then used to determine the orbital and EDR classes of each object.

4.2. Results

The above procedure was implemented for the binning definitions described in Tables 1, 2 for the ~ 2000 SP payload objects, and Vimpel objects with available ephemerides, in March 2018. The orbital regimes were further refined to form the GEO (including GEO, EGO, IGO, GHO, HAO), HEO (HEO, GTO, LMO), MEO (MEO, MGO) and LEO (LEO), from Table 3.

Figure 4 shows the proportion of each binning regime present in the datasets. As the EDR is a dynamic quantity which depends on orbital and solar conditions, this represents a snapshot of the population. The median LUPIs for each, annotated per bin, are generated from a post-processed dataset. Objects were excluded where the OD process did not properly converge (high level RMS exceeded), or where there was insufficient data for statistical outlier analysis (rapid state drift). For both SP and Vimpel, approximately 25% of the initial population was filtered.

It would be expected that objects in the GEO regime should obtain a better fit to the ODIN force model, due to the simplified dynamics. Here, the altitude is such that

SRP effects dominate those of atmospheric drag. However, it was the aggregated GEO regime that had the most varied distribution in LUPI. The orbital regimes were therefore considered with a higher level of fidelity. The resulting distributions are shown in Figure 5.

For Vimpel, the initial filtering mostly effected the IGO regime, where 90% of objects were removed due to an early drift in the C_r coefficient determination. HEO orbits suffered a 50% filtering due to high residuals, and for LMO in the high drag regime, 26% of objects were removed due to C_d drift. The remaining bin that appears to need special investigation in Figure 5, is that of the EGO regime. In this case, 10% of the population that survive pre-processing, experience C_r drift at a later time, resulting in the long tail of the distribution.

The SP dataset was similarly affected in the cases of LMO, HEO, and IGO. In the GTO and LEO high drag regimes, $\sim 30\%$ are filtered due to early C_d drift. The extended tail in the GEO and EGO regions are again caused by a remaining 19 and 13% for which C_r drift does not occur early in the fitting.

A Kolmogorov-Smirnov test was then performed in pairs to determine whether the LUPI intervals were statistically different to each other. This was performed under the null hypothesis, H_0 , that two independent samples are drawn from the same continuous distribution. Bins in which less than 10 data points were present were excluded. The distributions for the low drag regime are displayed in Figure 5, and the pairs for which H_0 could be rejected with a probability value of over 90% are discussed below.

For the Vimpel objects, the bin distributions of GEO and EGO could be statistically discerned, as well as GTO from HEO. MEO type distributions were indistinguishable with respect to any other orbit, as were any differences in drag regime.

For the SP payload objects, LEO could be differentiated from all other main orbital regimes for EDR 0. GEO, EGO and GTO were all also individually distinguishable. However, no statistical difference was present between high and low drag regimes for LEO. Only when LEO and LMO were aggregated into a larger LEO grouping, did the effects of EDR become detectable.

The same approach was applied to the SRP susceptibility (Table 2), for EDR bin 0. For both SP and Vimpel data, neither was seen to be discernible between orbital regimes. For the SP data, this may be explained due to the emphasis on rocket bodies in the development of the binning scheme [6].

To conclude, statistical testing shows that higher fidelity orbital classes give more discernible results than using EDR or SRP classes. Despite this, the median values per bin are very similar, as they are robust to objects with C_d or C_r drift, which are not removed during initial filtering. This pre-filtering does not affect 75% of objects, and additionally there is no single orbital regime which requires special attention. It can be seen that the median LUPI

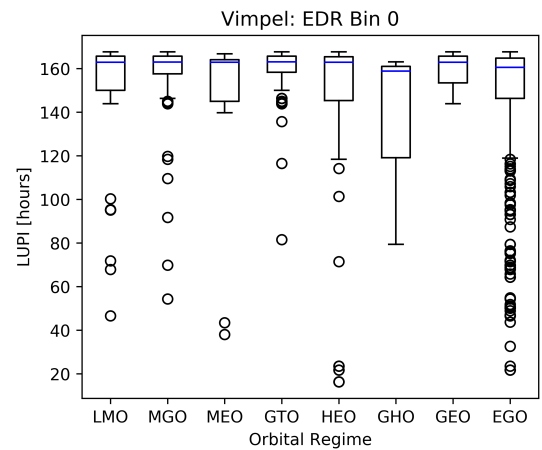
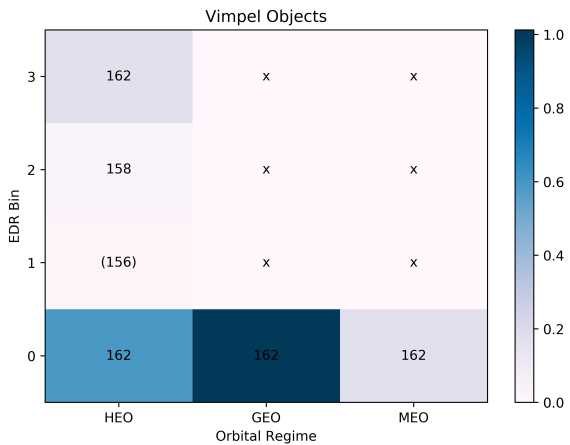
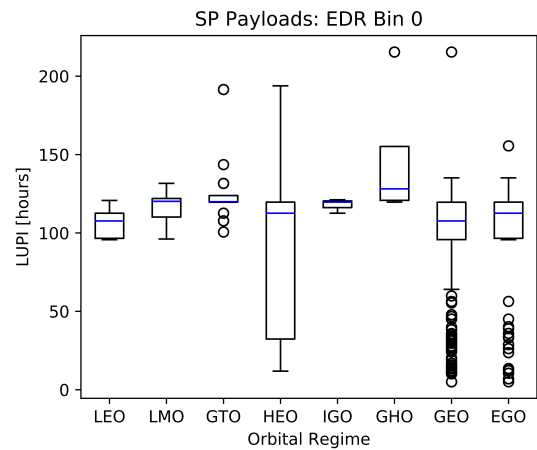
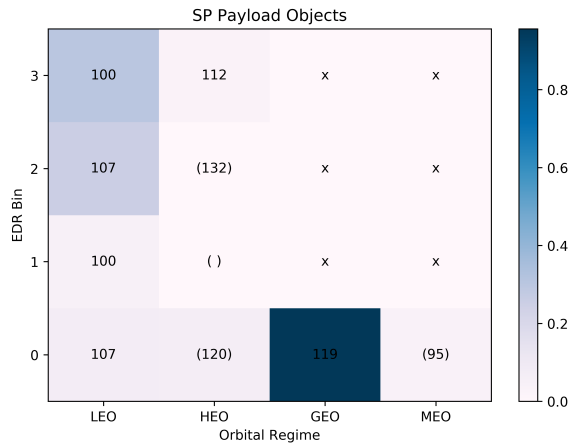


Figure 4. Histograms in EDR and orbital class bins. Colour scaling represents the proportion of objects residing in each bin, and the annotated numbers indicate the median optimised LUPI for that bin, having performed a filtering on the data. ‘x’ denotes impossible regions, and brackets are used to give results for bins with less than 10 data points. SP Payload objects (2147) with known mass, minimum cross section $> 1 \text{ m}^2$ taken from the DISCOS database. Vimpel objects (2422) with given ephemerides released in the week of 19/3/18.

Figure 5. Box plots for the distribution of optimum LUPI when grouped by orbital class, for EDR 0. The uncertainty box contains the 25th and 75th percentile, with the median denoted by the horizontal blue line. Whiskers correspond to the 10th and 90th percentile. Regions with less than 10 data points were excluded.

has a high dependence on the length of the dataspan: all Vimpel objects have a dataspan of 168 hours; typical SP spans are in the range of 115-135 hours.

5. CATALOGUE DATA FUSION

Once the state vector estimates and covariances have been obtained for a given object over all associated datasets (using their respective optimum LUPIs), they may be fused to give a final cataloguable state. Covariance intersection was chosen as the method for this fusion, as it offers a simple approach to obtaining the optimal weightings of each dataset.

5.1. Covariance Intersection

Covariance intersection (CI) is an efficient and extensively used algorithm in the field of multi-sensor data fusion as it does not require knowledge of cross correlations between signal sources.

The process provides a general framework for data fusion under uncertain conditions as it yields consistent estimates for any degree of cross correlation, and thus is also applicable to the fusion of catalogues of unknown generation parameters.

CI considers the intersection of two or more Gaussian distributions, individually characterised by some mean, \bar{x} and covariance P . The resulting fused mean and covariance is given by the following,

$$P_{fused} = \left[\sum_{i=1}^L \omega_i P_i^{-1} \right]^{-1} \quad (7)$$

$$\bar{x}_{fused} = P_{fused} \sum_{i=1}^L \omega_i P_i^{-1} \bar{x}_i \quad (8)$$

where w determines the weightings of the individual distributions under the constraints,

$$\sum_{i=1}^L \omega_i = 1, \omega_i \leq 0 \quad (9)$$

w can be specified, or chosen such that the accuracy of the resulting fused state outperforms that of the input parameters. This may be achieved by minimising an appropriate cost function such as the determinant or trace, Tr , of the fused covariance, to minimise the mean-square error of the output [3], i.e.,

$$\min_{\omega_i} [\text{Tr}(P_c)] \quad (10)$$

where a constrained optimiser can be used for higher dimensions to derive the optimal weighting coefficients.

The resulting estimate is a conservative upper bound that has the advantage of being robust with respect to unknown correlations, and also has a strictly non-increasing covariance according to the chosen weighting.

5.2. Fusion of Correlated SP and Vimpel Data

The above approach is considered for the sub-set of objects for which both SP and Vimpel ephemerides are available. To implement CI as an approach to the fusion of the two datasets, the state vector estimations and covariances must be provided at same epoch.

The first problem to consider, is the artificial nature of the covariance provided by the OD fitting process. Due to the correlation of errors in the ephemerides, the covariance is forcibly damped as the OD arc length increases.

One method to combat this effect would be to down-sample the data. However, the differing number of measurements in the two datasets, due to different measurement frequencies and data spans, will nevertheless force favour with the higher sampled set. To avoid this problem, a sample covariance for each object was derived over several sets of ephemerides.

To ensure consistency between the two datasets, an OD fit was first performed for each measurement file, using the derived optimum LUPI for the object. This state was

then propagated seven days into the future, to account for the shorter data span of the SP data. Only the set of SP ephemerides closest to the original OD epoch of each Vimpel set was considered. This introduces a secondary issue, in the form of an intrinsic preference, as the common epoch will necessarily be closer to the original propagation epoch of one dataset, usually the SP, rather than the other.

The error at the overlapping epochs, where new data becomes available after the 7 day propagation, is then sampled to generate a more realistic covariance. These covariances may then be applied to the optimisation problem in Equation 10 to derive an appropriate weighting for the fusion. Subsequently, the process may be reversed to find the sample covariance for the new fused state.

Here, the above methodology was applied to the GTO rocket fragmentation debris (CZ-3C) (NORAD 39352, Vimpel ID 066004) over a 6 month period.

The issues encountered with fitting to SP data in the atmospheric drag regime should be alleviated in the GEO region as a result of a simplified force model. In this regime, it is therefore expected that the residuals should overlap well, as can be seen in Figure 6. It is difficult to tell from this whether one set out-weighs the other due to the shorter dataspan of the SP data, and whether the atmospheric effects in the perigee of the orbit are apparent.

The sample (1σ) covariance ellipses generated from the datasets, and that of the resultant fused state, are shown in Figure 7. In this case, the covariance from the consolidated state can be seen to exceed the SP data, despite a heavy weighting towards it. However, an increase in covariance volume is not necessarily a negative result. A small sample covariance indicates that the derived orbit is self-consistent. As such, any persistent bias throughout the measurement data or model would be unidentifiable through the covariance. A fused state merely contains more information, though a reference orbit, or third independent source, would be required for any further knowledge to be extracted.

6. CONCLUSIONS & FUTURE WORK

A framework was developed for deriving a unified space object catalogue from data of different formats, frames and force models. For this study, CSpOC Special Perturbation (SP) data and JSC Vimpel data were considered.

For fusing complementary measurements, the method of covariance intersection was investigated. First, an estimate of the orbital state and a measure of its covariance must be obtained by refitting data, from any given catalogue, to a common force model. To up-scale this process for whole catalogues, representative LUPIs, for the OD processing, were explored for subclasses of objects. Binning schemas that account for differences in orbital regimes, drag effects (arising from the physical proper-

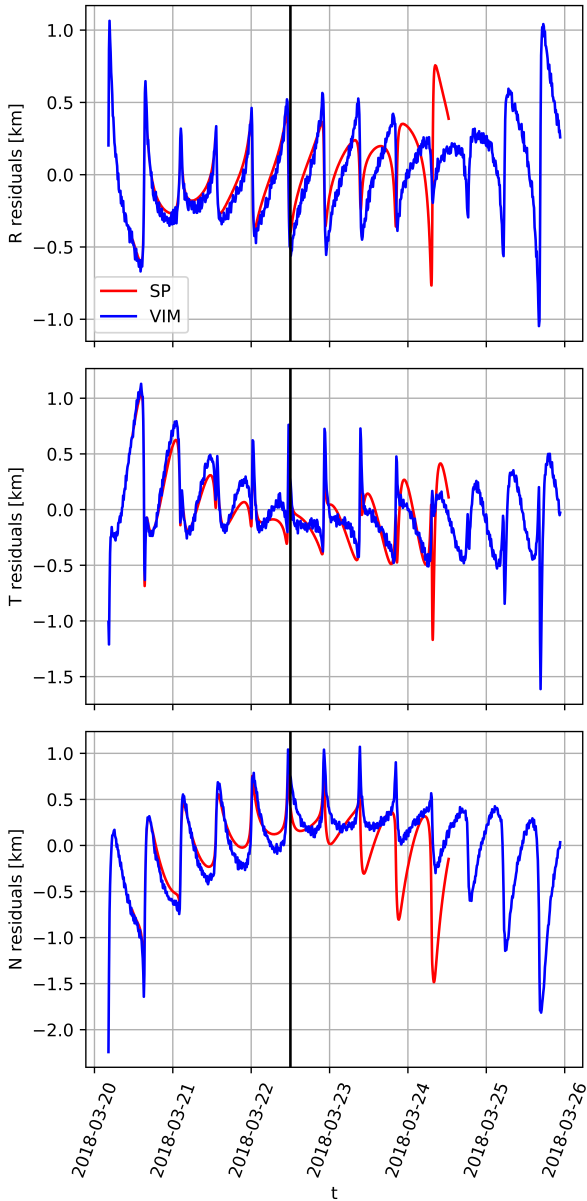


Figure 6. OD residuals, in the RTN frame, for NORAD object 39352, using both SP and Vimpel ephemerides, with the common OD epoch denoted by a vertical line.

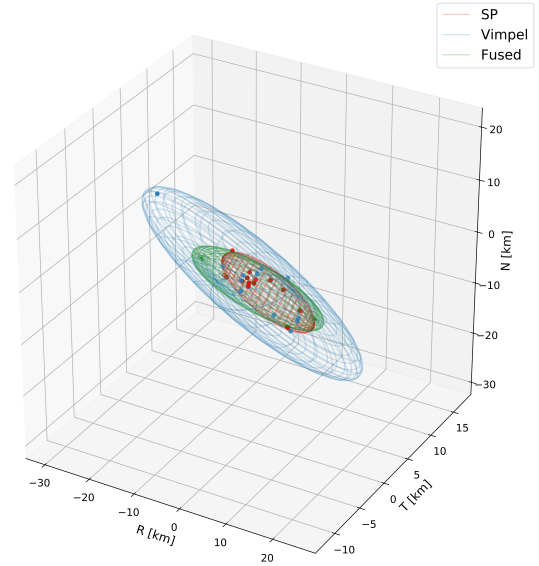


Figure 7. Sample covariance ellipsoids for SP data, Vimpel data and their cumulative fused state using measurement data over a 6 month period for NORAD object 39352.

ties of the objects as well as that of the atmosphere, using the EDR), and SRP effects, were implemented.

An optimal LUPI was calculated per bin, using a population of representative objects. These were obtained by pre-filtering the data against state drift and OD non-convergence, culminating in 75% of the original set. Statistical testing showed that higher fidelity orbital classes give more discernible results than those which implement EDR or SRP measures. Despite this, the median values per bin were very similar, and no single orbital regime stood out as requiring special attention. The resultant LUPIs have a high dependence on the length of the data span, which is a positive result for both SP and Vimpel data, as the optimal span exceeds or approaches the data update frequency, respectively.

Using this optimised OD control, covariance intersection was then performed for a GTO test case. SP and Vimpel data, with similarly matching residuals, were fused using derived sample covariances. However, in order to perform an assessment of the increase in accuracy of this resultant fused state, a reference orbit, or third independent source, would additionally be required.

The ultimate aim of the work is to integrate fused states, of complementary catalogues, into the DISCOS database. This would allow reference populations for debris evolution models to be updated, which may be particularly pertinent to the GEO regime, as can be seen in Figure 1. In future work, the framework should therefore be expanded to consider other datasets and catalogues, such as that of SP rocket bodies or laser ranging data.

REFERENCES

1. Alarcón, J. R., Klinkrad, H., Cuesta, J., & Martínez, F. M. (2005). Independent orbit determination for collision avoidance, 4th European Conference on Space Debris, Darmstadt, Germany
2. Berger J. M., et al., (1992). An Analysis of USSPACECOM's Space Surveillance Network Sensor Tasking Methodology, Master's Thesis, Air Force Institute of Technology
3. DeMars K. J., McCabe J. S., (2014). Multi-Sensor Data Fusion in Non-Gaussian Orbit Determination, AIAA/AAS Astrodynamics Specialist Conference, San Diego, California, United States
4. ESA Space Debris Office, (2018). ESA's Annual Space Environment Report, https://www.sdo.esoc.esa.int/environment_report/Space_Environment_Report_latest.pdf
5. Hejduk M. D., (2008). Space Catalogue Accuracy Modeling Simplifications, AIAA/AAS Astrodynamics Specialist Conference, Honolulu, Hawaii
6. Hejduk M. D., Ghrist R. W., (2011). Solar Radiation Pressure Binning for the Geosynchronous Orbit, AIAA/AAS Astrodynamics Specialist Conference, Girdwood, Alaska, United States
7. JSC Vimpel Data Portal, Orbit parameters of newly detected HEO space debris objects, <http://spacedata.vimpel.ru/>
8. Mclean F., (2017). DISCOS 3: An improved data model for ESA's Database and Information System Characterising Objects in Space, 7th European Conference on Space Debris, Darmstadt, Germany
9. Miller J. G., (2007). A New Sensor Allocation Algorithm for the Space Surveillance Network, Military Operations Research, Vol. 12, No. 1
10. Montenbruck O., Gill E., (2000). *Satellite Orbits: Models, Methods and Applications*, Springer, ed. 1
11. Stoll E., Merz K., Krag H., D'souza B., Bastida Virgili B., (2013). Collision Probability Assessment for the RapidEye Satellite Constellation, 6th European Conference on Space Debris, Darmstadt, Germany
12. Storz M. F., et al., (2002). High Accuracy Satellite Drag Model (HASDM), AIAA/AAS Astrodynamics Specialist Conference, Monterey, California, United States